Research Article GU J Sci, Part A, 13(3): 1239-1257 (2026) 10.54287/gujsa.1979919

Gazi University
Journal of Science
PART A: ENGINEERING AND INNOVATION
http://dergipark.org.tr/gujsa

The Role of Electrode Position in Gas Sensing and Charge Transport in ZnO Thin Films

Ahmad AJJAQ[1*]

1 Department of Basic Sciences, Faculty of Engineering and Natural Sciences, Ankara Yıldırım Beyazıt University, 06010, Ankara, Türkiye

Keywords

ZnO Thin Film
IDT Configuration
Gas Sensing
Charge Transport
Impedance Spectroscopy

Abstract

The influence of electrode positioning on the gas-sensing and charge-transport properties of ZnO thin films remains insufficiently explored despite its importance in resistive sensor design. Here, ZnO thin-film NH_3 sensors incorporating top-, bottom-, and hybrid-interdigitated electrode configurations (T-IDT, B-IDT, and H-IDT) were systematically compared under identical synthesis, device geometry, and measurement conditions. Sol–gel spin-coated ZnO films exhibited a polycrystalline hexagonal wurtzite structure, homogeneous elemental distribution, and continuous morphology. Electrical measurements revealed approximately linear I–V characteristics, while equivalent-circuit analysis of the impedance spectra demonstrated configuration-dependent resistive and relaxation behavior, with B-IDT exhibiting the most complex electrical response. Gas-sensing measurements toward 50 ppm NH_3 showed a strong dependence on electrode position, with responses at 230°C reaching 163%, 147%, and 106% for B-IDT, H-IDT, and T-IDT, respectively. Quantitative t_{90} analysis further revealed that the response/recovery dynamics depend on both electrode configuration and operating temperature, indicating that no single electrode configuration consistently provides the fastest dynamic response under all conditions. Repeated exposure–recovery measurements demonstrated stabilization of the sensing response after initial cycling, while concentration-dependent measurements over 5–200 ppm NH_3 produced systematic response increases for all configurations. These findings demonstrate that electrode positioning governs how gas-induced conductivity changes are electrically sampled within the same ZnO sensing layer, producing a practical trade-off between response magnitude, resistance, and dynamic behavior. Electrode positioning therefore represents a simple device-level design parameter for tailoring the performance of resistive metal-oxide gas sensors.

Cite

Ajjaq, A. (2026). The Role of Electrode Position in Gas Sensing and Charge Transport in ZnO Thin Films. *GU J Sci, Part A*, *13*(3), 1239-1257. doi:10.54287/gujsa.1979919

Author ID (ORCID Number)

0000-0002-2136-3965 Ahmad AJJAQ

Article Process

Submission Date	26.06.2026
Revision Date	17.07.2026
Accepted Date	01.09.2026
Early Pub Date	28.09.2026
Published Date	30.09.2026

1. INTRODUCTION

Metal oxide semiconductor (MOS) gas sensors have attracted considerable attention owing to their simple fabrication, low cost, high sensitivity, and suitability for real-time environmental and industrial monitoring. Among various MOS materials, zinc oxide (ZnO) has been widely investigated because of its wide band gap, chemical stability, high electron mobility, and favorable surface reactivity (Çağırtekin & Acar, 2026). Its gas-sensing behavior is primarily governed by surface adsorption/desorption processes that modulate charge carrier concentration and, consequently, the electrical resistance of the sensing layer.

*Corresponding Author, e-mail: aajjaq@aybu.edu.tr

This work is licensed under Creative Commons Attribution 4.0 International.

GU J Sci, Part A | 13(3) 1239-1257 (2026) | 10.54287/gujsa.1979919

Strategies for improving ZnO gas-sensor performance have predominantly focused on modification of the sensing material itself, including elemental doping (Soltabayev et al., 2022), catalyst decoration (Vuong et al., 2016), morphology engineering (Fioravanti et al., 2021), and optimization of synthesis conditions (Mokrushin et al., 2025). However, the measured response of a resistive gas sensor is determined not only by the intrinsic properties of the sensing material but also by how the gas-induced conductivity change is electrically sampled through the electrodes. In this context, electrode design represents an important device-level parameter because it defines the electrode–film interface and the effective pathway through which charge carriers are collected. Interdigital electrodes (IDTs) are particularly attractive because they provide a large electrode–sensing-layer contact area within a compact device geometry (Lee, 2017).

Previous studies provide increasing evidence that electrode design can influence gas-sensor performance through several geometrical and spatial parameters. Öztürk et al. (2013) investigated the effect of electrode position in hydrothermally grown ZnO nanorod sensors by placing Au interdigitated electrodes either above or below the sensing layer and demonstrated that electrode placement influences NO_2-sensing characteristics. Chen et al. (2015) subsequently examined interelectrode spacing in ZnO nanorod-based NH_3 sensors and found that decreasing the IDT spacing increased the sensor response, which was associated with the formation of more cross-linked conduction pathways between the electrodes. In the same year, Cui and Murray (2015) showed in Au/YSZ/Au solid-electrolyte NO sensors that electrode configuration can alter gas-diffusion and ionic-transport pathways, as revealed by impedance spectroscopy and equivalent-circuit analysis. Prajesh et al. (2018) more directly compared Pt interdigitated electrodes positioned above and below a sputtered SnO_2 sensing film and reported an approximately twofold higher NH_3 response for the top-electrode configuration. Their experimental and simulation results primarily associated this enhancement with the gas-concentration and diffusion profiles through the sensing layer and the stronger contribution of conductivity changes near the exposed film surface. Notably, a different trend is observed in the present ZnO system, where the bottom IDT configuration exhibits both a higher baseline resistance and a stronger NH_3 response than other designed configurations. This contrast indicates that the influence of electrode placement is coupled to the charge-transport characteristics of the sensing layer and cannot be explained solely by electrode proximity to the gas-exposed surface. Wei et al. (2020) further demonstrated the importance of electrode dimensions in printed polymer-based resistive gas sensors by systematically varying the width and gap of silver (Ag) interdigitated electrodes, with smaller electrode gaps producing greater sensitivity toward ethanol and methane. More recently, Huang, C.-Y. et al. (2024) demonstrated that electrode asymmetry can itself be exploited as a device-design parameter; increasing the width ratio of asymmetric Au IDTs from 1 to 3 in amorphous InGaZnO ozone sensors increased the self-powered gas response from approximately 0 to 60%. Konuk Ege et al. (2026) additionally investigated the influence of IDT finger number in PANI-based NH_3 sensors while maintaining a constant interelectrode spacing and observed the largest resistance change for the configuration containing the greatest number of fingers, although the overall effect of electrode geometry was considered secondary to that of the sensing layer.

GU J Sci, Part A | 13(3) 1239-1257 (2026) | 10.54287/gujsa.1979919

Collectively, these studies establish that the electrode is not merely a passive electrical contact; its geometry and spatial relationship with the sensing layer can directly influence the measured sensor characteristics. Nevertheless, previous investigations have largely addressed individual design parameters –such as spacing, finger geometry, asymmetry, or conventional top/bottom placement– rather than systematically examining how fundamentally different electrode positions reshape the electrical conduction pathway within the same sensing layer. In particular, the intermediate case represented by a hybrid configuration, in which the two opposing electrodes contact different sides of the sensing film, remains unexplored. Furthermore, the connection between such spatial electrode configurations and their underlying frequency-dependent charge-transport behavior has not been systematically established.

Motivated by this gap, the present work isolates electrode position as the principal device-design variable and systematically investigates its influence on the gas-sensing and charge-transport properties of sol–gel spin-coated ZnO thin films employing Ag IDTs. Three distinct configurations are directly compared: top-IDT (T-IDT), bottom-IDT (B-IDT), and hybrid-IDT (H-IDT), with the latter positioning the two opposing electrodes on different sides of the ZnO layer. Importantly, the devices are derived from the same ZnO processing route and employ identical electrode geometry and measurement conditions, enabling differences in electrical and sensing behavior to be attributed primarily to electrode positioning rather than to changes in sensing-material composition or device dimensions. DC electrical characterization and gas-sensing measurements are complemented by impedance spectroscopy to probe how each configuration modifies the effective charge-transport pathway through the film. This combined approach moves beyond a performance-only comparison and provides a transport-based interpretation of why electrode position alters the measured sensing behavior. The findings therefore establish electrode positioning as a practical device-level design parameter for tailoring the electrical transport and sensing characteristics of ZnO thin-film resistive gas sensors.

2. MATERIALS AND METHODS

2.1. Preparation of ZnO Thin Films

Microscope glass substrates (25 mm × 25 mm) were used for sensor fabrication. Prior to deposition, the substrates were sequentially cleaned in acetone, ethanol, and deionized water in an ultrasonic bath for 15 min in each solvent. The cleaned substrates were then dried under a dry air stream and treated on a hot plate at 100°C for 10 min to remove residual moisture.

The ZnO precursor solution was prepared using zinc acetate dihydrate [$Zn(CH_3COO)_2 \cdot 2H_2O$] as the zinc source and methanol as the solvent. Monoethanolamine (MEA) was employed as a stabilizing agent to improve solution homogeneity and regulate hydrolysis during film formation. A 0.5 M precursor solution was obtained by dissolving zinc acetate dihydrate in methanol under continuous magnetic stirring at 60°C. The molar ratio of MEA to zinc acetate was maintained at 1:1. The resulting transparent solution was stirred for 2 h and subsequently aged at room temperature for 24 h to ensure complete dissolution and stabilization.

GU J Sci, Part A | 13(3) 1239-1257 (2026) | 10.54287/gujsa.1979919

ZnO thin films were deposited by the spin-coating technique, as illustrated in Figure 1a. Approximately 100 µL of precursor solution was dispensed onto the substrate surface and spun at 3000 rpm for 30 s. After each coating cycle, the deposited layer was preheated on a hot plate at 150°C for 10 min to evaporate residual solvent and promote the decomposition of organic species. This coating–preheating sequence was repeated for a total of 10 cycles for all three device configurations (T-IDT, B-IDT, and H-IDT). The number of coating cycles and all associated deposition and processing parameters were kept identical across the three configurations to minimize fabrication-related variations and enable a direct comparison of the effect of electrode positioning. The multilayer deposition was employed to ensure reliable electrical measurements by electrically isolating the top and bottom silver (Ag) electrodes (particularly for H-IDT configuration), thereby minimizing leakage currents and also preserving the intended electrode configuration.

Following the final coating cycle, all samples were annealed in air at 500°C for 1 h using a heating rate of 5°C/min. The post-deposition annealing treatment promotes the crystallization of the ZnO phase and the removal of residual organic compounds. After annealing, the samples were allowed to cool naturally to room temperature inside the furnace. Following ZnO deposition and annealing at 500°C, no visible delamination or discontinuity of the Ag electrodes was observed in any of the sensor configurations, particularly in the B-IDT device, whose electrodes were subjected to these subsequent processing steps.

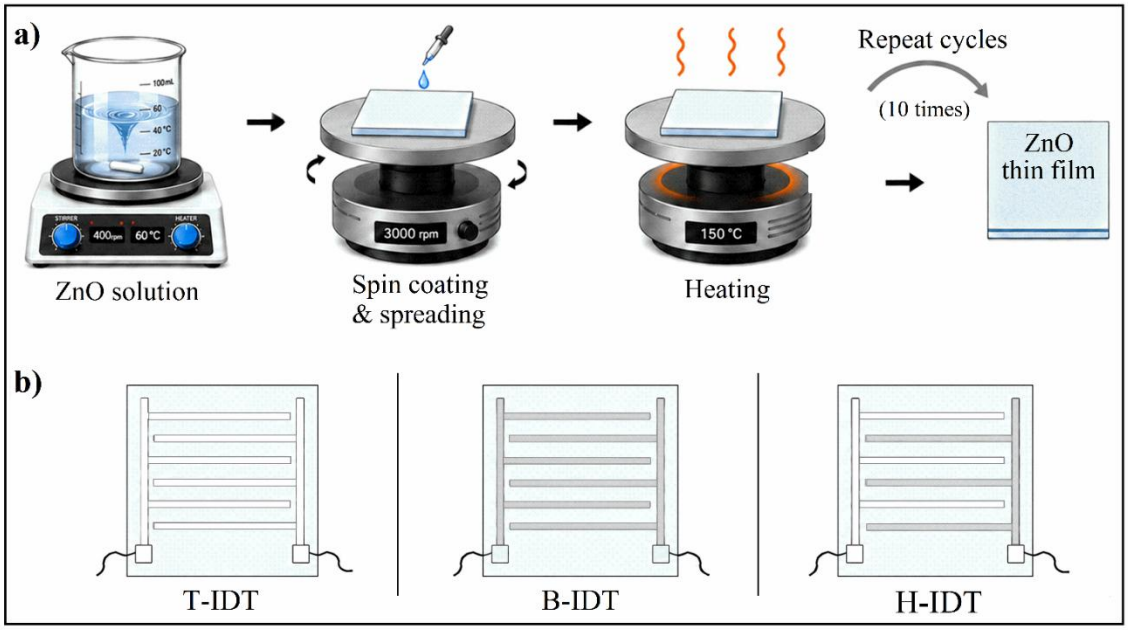

Figure 1. a) *Overview of the ZnO thin-film fabrication procedure and* ***b)*** *the three sensor platforms designed to investigate the influence of electrode positioning on device performance.*

2.2. Fabrication of Electrode Configurations

Three distinct electrode configurations were fabricated to investigate the influence of current-collection pathways on the gas-sensing performance and charge-transport characteristics of ZnO thin films (Figure 1b). In the top interdigital-electrode configuration (T-IDT), the ZnO thin film was initially deposited on the glass substrate, after which the Ag interdigital pads were formed on the film surface. In the bottom interdigital-

GU J Sci, Part A | 13(3) 1239-1257 (2026) | 10.54287/gujsa.1979919

electrode configuration (B-IDT), contact pads were first deposited onto the glass substrate, followed by the deposition of the ZnO sensing layer. A third configuration, denoted as the hybrid interdigital-electrode (H-IDT), was designed by positioning one electrode pad and its corresponding fingers beneath the ZnO layer, while the opposing electrode pad was deposited on the film surface. This unique arrangement establishes a mixed conduction pathway involving both surface and bulk regions of the sensing layer while eliminating the possibility of direct electrical short-circuiting between the electrodes. The three configurations were fabricated using identical ZnO deposition conditions to ensure that any observed differences in sensing and electrical behavior originated primarily from electrode positioning.

Silver electrodes were deposited by thermal evaporation using a high-vacuum coating system (Vac Coat Ltd.) through a stainless-steel shadow mask. High-purity Ag (>99.99%) was deposited at a base pressure of approximately 5×10^{-6} Torr and a deposition rate of approximately 0.2 nm/s, monitored using a quartz-crystal thickness sensor, until a final thickness of approximately 150 nm was achieved. The substrates were maintained at room temperature during deposition. The interdigital electrode geometry consisted of two opposing comb-like electrodes containing three fingers on each side. Each finger had a width of 200 μm and a length of approximately 4 mm, with a spacing of 200 μm between adjacent fingers. The active sensing area defined by the electrode structure was approximately 15 mm × 15 mm. Following electrode deposition, the samples were heat-treated at 200°C for 30 min in air to improve electrode adhesion and electrical stability, and to promote reliable Ohmic contact behavior between Ag and ZnO. Electrical contacts were established using conducting silver paste and copper wires attached to the electrode pads.

2.3. Characterization and Data Analysis

The crystal structure of the ZnO thin films was analyzed by X-ray diffraction (XRD) using Cu Kα radiation (λ = 1.5406 Å). Surface morphology and film uniformity were examined using field-emission scanning electron microscopy (FE-SEM). The thickness and continuity of the deposited films were additionally evaluated from cross-sectional SEM images. For structural and morphological characterization, a separate ZnO thin film was prepared under identical synthesis and annealing conditions. Since all sensor devices were fabricated from the same precursor solution following the same deposition protocol, the XRD and SEM results obtained from the reference sample were considered representative of the sensing layers employed in all device configurations.

Gas-sensing measurements were carried out in a stainless-steel test chamber (internal volume ~300 mL) equipped with gas inlet and outlet ports. The temperature controller, gas-flow controllers, and electrical measurement units were integrated into a computer-controlled system and operated through a LabVIEW-based interface. The operating temperature was regulated using an SRS-CTC100 temperature controller (Stanford Research Systems) where measurements were performed from 30 to 230°C in 20°C increments. The sensor resistance was continuously recorded using a Keithley 2400 Sourcemeter under a constant bias voltage of 3 V. Prior to each measurement, the sensor was stabilized under dry synthetic air at the selected operating temperature for approximately 15 min, and data acquisition was initiated after the sample-holder temperature

GU J Sci, Part A | 13(3) 1239-1257 (2026) | 10.54287/gujsa.1979919

stabilized within ±0.05°C of the set value. The target gas (high-purity NH_3, >99%) was supplied from a certified gas cylinder, while dry synthetic air served as both the carrier and reference gas. Gas delivery was controlled using two high-precision mass flow controllers (MFCs, MKS Instruments), with operational ranges of 0–500 sccm for dry air and 0–5 sccm for NH_3. The respective flow rates were adjusted through the LabVIEW-based control system to generate the intended ppm of NH_3 gas while maintaining a total gas flow rate of approximately 500 sccm throughout the sensing measurements. Considering the chamber volume and the maintained total gas flow rate, the nominal gas residence time ($\tau = V/Q$) was estimated to be approximately 35 s. The sensor response (S) was calculated according to $S\ (\%) = [(R_a–R_g)/R_{min}]\times100$, where R_a and R_g represent the sensor resistance in air and upon exposure to NH_3, respectively, and R_{min} corresponds to whichever of R_a or R_g is lower. The response and recovery times were calculated based on the t_{90} criterion, defined as the time required to reach 90% of the total resistance change following gas exposure and to recover 90% of the initial resistance after removal of the target gas, respectively.

The objective of this study was not to optimize ZnO sensing performance toward a specific analyte, but to isolate and evaluate the influence of IDT positioning on the electrical and sensing behavior of the devices. Accordingly, all sensing and measurement conditions were kept constant across the three configurations, with electrode positioning as the principal device-design variable. NH_3 was selected as a model target gas based on the well-established sensitivity of ZnO toward ammonia, and a fixed concentration of 50 ppm was used for the primary comparative measurements. Relative humidity was not independently varied or controlled. Although humidity can influence MOS gas sensing by modifying the baseline resistance and competing with oxygen and target-gas molecules for surface adsorption sites (Tereshkov et al., 2024), it was not introduced as an additional experimental variable. Similarly, selectivity toward interfering gases was not investigated. Further evaluation under controlled humidity and in the presence of potential interfering gases will therefore be required to establish the performance of these configurations under practical NH_3-sensing conditions.

Electrical impedance spectroscopy measurements were performed in ambient atmosphere to investigate the influence of electrode positioning on the charge transport mechanisms of the ZnO thin-film sensors. The measurements were carried out using an impedance analyzer (Keysight E4990A) over a frequency range of 20 Hz–10 MHz. An AC excitation voltage of 50 mV was applied during all measurements to ensure operation within the linear response regime. The obtained spectra were analyzed using Nyquist ($-Z''$ vs. Z') representations to evaluate the frequency-dependent electrical behavior of the devices. Equivalent-circuit modeling was subsequently performed to quantify the resolved electrical relaxation processes and evaluate their dependence on electrode configuration.

3. RESULTS AND DISCUSSION

3.1. Structural Analysis

As shown in Figure 2a, the EDS spectrum reveals only Zn and O signals, with no detectable impurity elements except for a weak C signal, which is commonly attributed to environmental exposure. The corresponding

GU J Sci, Part A | 13(3) 1239-1257 (2026) | 10.54287/gujsa.1979919

elemental mapping (inset of Figure 2a) also confirms the uniform distribution of Zn and O across the film surface. The XRD pattern (Figure 2b) shows that the film crystallizes in the hexagonal wurtzite ZnO phase, as evidenced by diffraction peaks in good agreement with JCPDS card No. 36-1451 and a pronounced preferential orientation along the (002) plane. No secondary phases are detected, supporting the successful formation of crystalline ZnO. These results confirm the successful synthesis of high-purity polycrystalline ZnO thin films, providing a reliable platform for investigating the influence of electrode positioning on gas-sensing and charge-transport characteristics. Moreover, the FE-SEM images shown in Figure 2c reveal a continuous, compact, and homogeneous ZnO thin film that fully covers the substrate surface without visible cracks or voids. The top-view micrograph shows a densely interconnected channel-like morphology, which is commonly observed in MEA-assisted sol–gel spin-coated ZnO films and has been reported previously (Barin et al., 2022; Demircan et al., 2022). The cross-sectional FE-SEM image indicates a nearly uniform film thickness of approximately 640 nm across different regions of the sample, demonstrating good deposition homogeneity and film integrity.

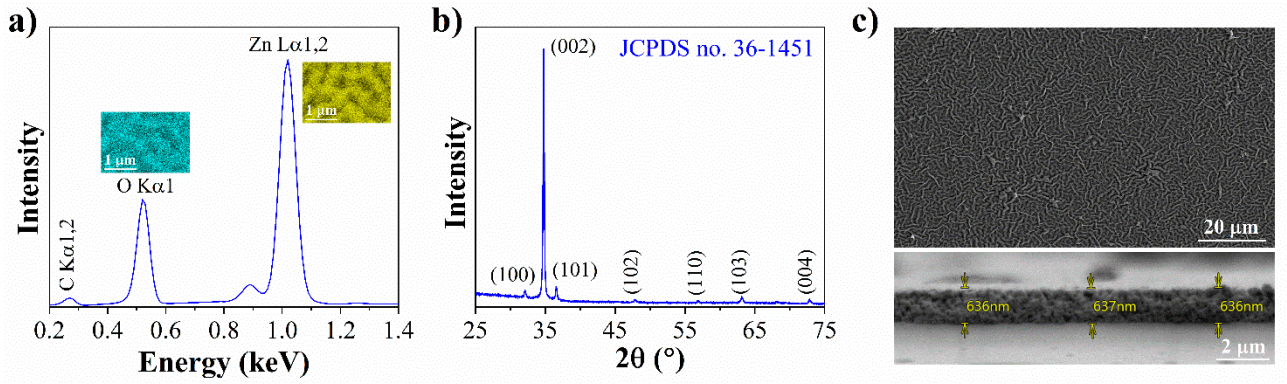

Figure 2. a) *EDS spectrum (inset: mapping),* ***b)*** *XRD pattern, and* ***c)*** *FE-SEM top- and side-view micrographs of the reference ZnO thin film synthesized under the same conditions as the sensing layers.*

3.2. Electrical Analysis

To establish a direct relationship between electrode configuration and electrical transport, the ZnO sensors were investigated using both steady-state (DC I–V) and frequency-resolved (AC impedance) techniques. As shown in Figure 3a, the I–V characteristics of the three ZnO sensors exhibit nearly linear and symmetric behavior over the investigated voltage range, indicating the formation of predominantly Ohmic Ag/ZnO contacts with negligible rectifying effects. However, the slopes of the I–V curves differ substantially depending on the IDT configuration, demonstrating that electrode positioning strongly influences the effective electrical conduction pathways. The T-IDT device exhibits the steepest slope and the highest current levels, corresponding to the lowest resistance (0.43 MΩ), implying that charge transport is dominated by less resistive regions located near the ZnO surface, consistent with a greater contribution from near-surface current pathways between the top electrodes. In contrast, the B-IDT configuration shows the smallest current response and the highest resistance (2.25 MΩ), suggesting that carriers traverse a more resistive pathway involving a larger fraction of the ZnO film layer. Such differences can be interpreted in terms of the relative contributions of sheet resistance and bulk resistivity, which are known to depend strongly on current-path geometry and

GU J Sci, Part A | 13(3) 1239-1257 (2026) | 10.54287/gujsa.1979919

electric-field distribution in semiconductor thin films (Schroder, 2006; Sze & Ng, 2007). The H-IDT sensor exhibits intermediate behavior (0.78 MΩ), consistent with the coexistence of surface- and bulk-mediated conduction pathways. These observations indicate that the electrical response of ZnO thin-film sensors can be effectively tailored through electrode design without altering the sensing material itself. The preserved electrical continuity and approximately linear I–V characteristics observed for all three configurations, particularly for the B-IDT device, whose Ag electrodes were exposed to subsequent ZnO deposition and annealing at 500°C, indicate that the Ag/ZnO contacts remained electrically functional after processing and did not exhibit strongly rectifying behavior. This suggests that the systematic differences among the devices are unlikely to be dominated by Schottky-type contact effects. Nevertheless, subtle nanoscale differences between the exposed and buried Ag/ZnO interfaces cannot be completely excluded because of their different fabrication sequences and the absence of direct cross-sectional characterization.

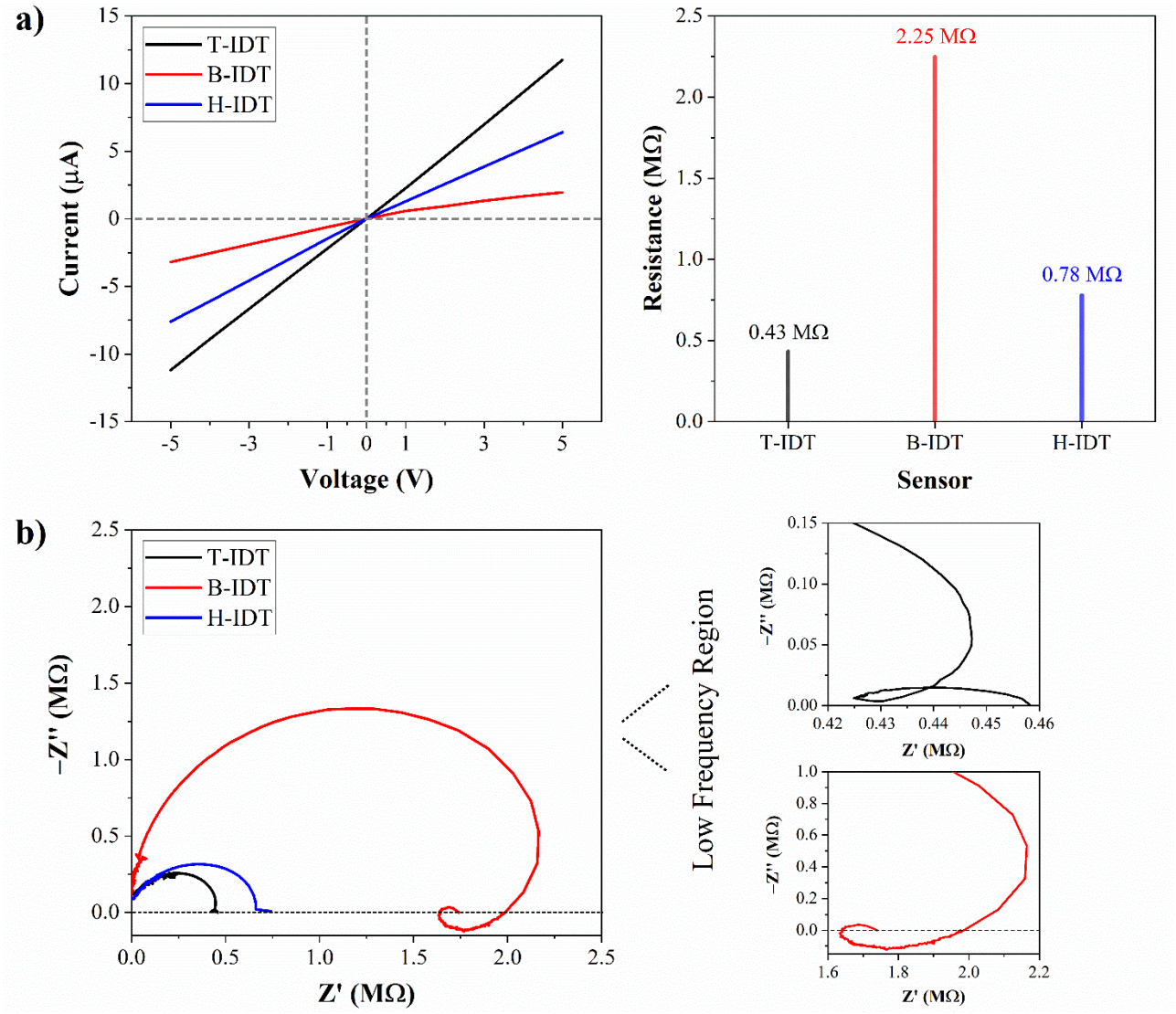

Figure 3. a) *Current–voltage (I–V) characteristics and* ***b)*** *Nyquist plots of the T-IDT, B-IDT, and H-IDT ZnO sensors measured at 30°C in ambient conditions. The Nyquist plots are presented as –Z'' versus Z', retaining the sign of the measured imaginary impedance component.*

GU J Sci, Part A | 13(3) 1239-1257 (2026) | 10.54287/gujsa.1979919

From a practical device perspective, the higher baseline resistance of the B-IDT configuration results in a lower operating current, requiring readout electronics with sufficient sensitivity and dynamic range for reliable signal acquisition (Cao et al., 2025). However, the higher resistance also reduces electrical power consumption under constant-voltage operation. At the applied bias of 3 V, the estimated baseline power consumption is approximately 4.0 μW for B-IDT, compared with 20.9 μW for T-IDT and 11.5 μW for H-IDT. Thus, the increased resistance of the B-IDT configuration represents a trade-off between readout requirements and reduced electrical power consumption.

The impedance spectroscopy results in Figure 3b further show that electrode positioning affects both the impedance magnitude and the relaxation behavior of the ZnO devices. To quantify these differences, the signed complex-impedance spectra were fitted using the minimum equivalent-circuit complexity required to reproduce the experimental response, with the resulting parameters summarized in Table 1. The use of R‖Q elements, where Q represents a constant phase element (CPE), accounts for the non-ideal capacitive response commonly observed in polycrystalline ZnO and enables the different relaxation contributions to be represented within the equivalent-circuit model. Similar CPE-based descriptions have been widely employed for polycrystalline ZnO systems (Balasubramani et al., 2019; Chuong et al., 2026).

Table 1. *Equivalent-circuit parameters obtained from fitting the signed impedance spectra of the T-IDT, B-IDT, and H-IDT ZnO sensors over the 20 Hz–10 MHz frequency range. R and Q denote the resistance and CPE coefficient, respectively, while f_c / τ represent the characteristic relaxation frequency / time. For B-IDT, R_i, Q_i, and L describe the additional inductive-type relaxation.*

Parameter	T-IDT	B-IDT	H-IDT
Equivalent circuit	R_s–(R‖Q)*	R_s–(R_c‖Q_c)–[(R_i+jωL)‖Q_i]	R_s–(R_1‖Q_1)–(R_2‖Q_2)
R / R_c / R_1 (kΩ)	~ 508	~ 928	~ 97
Q / Q_c / Q_1 (s^n/Ω)	~ 2.0×10^{-13}	~ 4.8×10^{-13}	~ 5.5×10^{-13}
f_c / f_{c1} (kHz)	1594	358	2979
τ / τ_1 (μs)	0.100	0.445	0.053
R_2 (kΩ)	–	–	~ 638
Q_2 (s^n/Ω)	–	–	~ 4.2×10^{-13}
f_{c2} (kHz)	–	–	592
τ_2 (μs)	–	–	0.269
R_i (MΩ)	–	~ 1.22	–
Q_i (s^n/Ω)	–	~ 6.0×10^{-13}	–
L (H)	–	~ 0.64	–
χ^2	1.44×10^{-2}	1.05×10^{-2}	9.19×10^{-3}

* The T-IDT spectrum shows a secondary capacitive shoulder, but it was not sufficiently resolved to justify stable independent fitting; therefore, only the dominant relaxation is reported quantitatively.

GU J Sci, Part A | 13(3) 1239-1257 (2026) | 10.54287/gujsa.1979919

The B-IDT device exhibited the largest overall resistive contribution, consistent with the DC measurements, and showed the most complex impedance response. In particular, its signed low-frequency response extends into the inductive region, requiring an additional inductive-type contribution in the equivalent circuit. Such a feature indicates a delayed electrical relaxation process superimposed on the dominant capacitive response; however, its microscopic origin cannot be uniquely identified from the present measurements. Inductive loops in impedance spectra can arise from interfacial or adsorption-related relaxation processes and therefore should not be assigned to a specific mechanism without independent evidence (Boukamp, 2001). The stronger complexity of B-IDT is nevertheless consistent with its buried-electrode geometry, for which the measured current must sample conductivity changes extending from the gas-active surface toward the underlying Ag/ZnO interface.

In comparison, the T-IDT spectrum was predominantly capacitive, with a secondary shoulder that was not sufficiently resolved for reliable independent parameter extraction. In contrast, the H-IDT spectrum was best represented by two R‖CPE relaxation contributions, indicating two distinguishable capacitive processes within the investigated frequency range. The differences in fitted resistances, characteristic relaxation frequencies and times, and circuit complexity among the three configurations provide quantitative evidence that electrode positioning modifies the electrical relaxation behavior and effective charge-transport pathways sampled within the same ZnO layer. These results further demonstrate that the electrical characteristics of the devices are governed not only by the intrinsic properties of ZnO but also by the spatial arrangement of the electrodes relative to the sensing layer.

3.3. Gas-Sensing Analysis

Representative transient resistance plots, together with the corresponding sensing response values presented in Figure 4, show that electrode positioning has a pronounced influence on the NH_3-sensing behavior of ZnO thin films. The response values were obtained from three repeated measurements on each device and are reported as mean values, with the corresponding standard deviations shown as error bars in Figure 4. All sensors exhibited measurable responses toward 50 ppm NH_3 over the investigated temperature range, with the response magnitude increasing markedly at higher operating temperatures. The maximum response was obtained at 230°C for all configurations. Among the three configurations, the B-IDT sensor consistently showed the highest mean response, increasing from 6% at 30°C to 40% at 130°C and 163% at 230°C. The H-IDT sensor showed intermediate values of 3%, 18%, and 147%, whereas the T-IDT sensor showed mean responses of 2%, –10%, and 106% at the same temperatures, respectively. This trend indicates that placing the electrodes beneath the ZnO sensing layer promotes stronger modulation of the effective conduction pathway during NH_3 exposure, while the hybrid configuration combines contributions associated with both top- and bottom-electrode current collection.

The enhanced response observed at 230°C can be associated with the temperature-dependent state and reactivity of oxygen species adsorbed on the ZnO surface. At relatively low temperatures, adsorbed molecular

GU J Sci, Part A | 13(3) 1239-1257 (2026) | 10.54287/gujsa.1979919

oxygen species such as O_2^- predominate, and the reaction between NH_3 and surface oxygen proceeds comparatively slowly, resulting in limited modulation of the electron concentration. As the temperature increases, thermally activated chemisorption and surface-reaction kinetics become more favorable, with more reactive ionic oxygen species, particularly O^-, contributing increasingly to the sensing process. At 230°C, the combination of enhanced oxygen activation, faster NH_3–oxygen surface reactions, and more efficient electron release back to the ZnO conduction band produces a larger change in resistance and hence a higher sensing response. The increased thermal energy also facilitates desorption and surface re-equilibration after removal of NH_3, consistent with the improved recovery observed at this temperature. At still higher temperatures, excessive desorption of oxygen and target-gas molecules may eventually reduce surface coverage and sensing response; therefore, 230°C is regarded here as the highest-response temperature within the investigated range rather than an absolute optimum.

The dynamic behavior further indicates that the response and recovery kinetics depend on both electrode configuration and operating temperature. The t_{90} response/recovery times for T-IDT, B-IDT, and H-IDT were approximately 0.39/0.44, 0.44/0.69, and 1.36/>2.09 min at 30°C; 1.12/>2.09, 1.62/>2.09, and 1.63/>2.09 min at 130°C; and 0.95/>2.09, 0.64/1.51, and 1.09/>2.09 min at 230°C, respectively. Where 90% recovery was not reached within the recorded purge interval, the recovery time is conservatively reported as >2.09 min rather than extrapolated beyond the measurement window. The incomplete and non-monotonic recovery with temperature reflects the competing effects of adsorption, surface reaction, desorption, and surface re-equilibration that govern ZnO-based NH_3 sensing (Hsueh & Ding, 2022; Hjiri et al., 2024).

While the temperature dependence of the response/recovery kinetics reflects changes in the underlying adsorption, reaction, and desorption processes, the differences observed among the three configurations are attributed primarily to their current-collection geometry rather than to intrinsically different NH_3 adsorption/desorption kinetics, since the ZnO surface and gas-exposure conditions are nominally identical. In T-IDT, the electrodes directly sample conductivity modulation near the gas-exposed surface where NH_3–oxygen reactions occur. In B-IDT, although NH_3 adsorption occurs at the same exposed surface, the resulting conductivity modulation must influence the conduction pathway extending toward the buried Ag/ZnO interface before being fully reflected in the measured current, while H-IDT combines features of both pathways. Thus, electrode placement modifies how surface-induced conductivity changes are electrically sampled rather than the intrinsic surface chemistry itself, consistent with previous reports on electrode and gas-access effects in thin-film gas sensors (Plecenik et al., 2015; Prajesh et al., 2018; Huang, B.-R. et al., 2024). From a practical perspective, these results reveal a trade-off between response magnitude and dynamic performance. The B-IDT configuration is advantageous when maximizing the measurable resistance change is prioritized, whereas configurations exhibiting shorter response/recovery times may be more suitable for real-time monitoring where rapid tracking of concentration changes is required. Importantly, the t_{90} results show

GU J Sci, Part A | 13(3) 1239-1257 (2026) | 10.54287/gujsa.1979919

that this trade-off is temperature dependent rather than being an intrinsic characteristic of a single electrode configuration.

A particularly important observation is the temperature-dependent response-polarity inversion exhibited by the T-IDT sensor. While the B-IDT and H-IDT sensors maintained a consistent response polarity throughout the investigated temperature range, this behavior was observed exclusively in the T-IDT sensor. Therefore, its response is presented at 20°C intervals over the 30–230°C range to clearly map the onset, evolution, and reversal of the polarity transition (Figure 4). At 30 and 50°C, NH_3 exposure produced a decrease in T-IDT resistance, consistent with the behavior of B-IDT and H-IDT. The response began to shift toward the opposite polarity at approximately 70°C, followed by a clear resistance increase from around 90°C. As the temperature increased further, the magnitude of this inverted response progressively diminished, and the resistance-decreasing behavior was restored within the 170–190°C range. Thus, unlike B-IDT and H-IDT, which consistently exhibited a decrease in resistance upon NH_3 exposure, T-IDT exhibits a well-defined intermediate-temperature regime characterized by reversible response-polarity inversion. Repeated measurements confirmed that this unusual temperature-dependent behavior is reproducible rather than an isolated measurement artifact. The reproducibility of the polarity transition, together with the absence of a comparable inversion in the B-IDT and H-IDT devices measured under identical conditions, makes simple baseline drift an unlikely primary origin. Although the approximately linear I–V characteristics indicate electrically functional Ag/ZnO contacts, a contribution from temperature-dependent interfacial effects cannot be completely excluded. Similar reversals in gas-response polarity have been reported in ZnO-based sensors and have been associated with changes in doping level, operating temperature, and gas concentration, reflecting shifts in the relative contributions of electron- and hole-mediated conduction pathways (Ajjaq et al., 2024, and references therein). In particular, the polarity inversion observed here may be associated with the surface-dominated conduction pathway of the T-IDT configuration, coupled with the temperature-dependent evolution of oxygen adsorption and surface-reaction kinetics on ZnO. Adsorbed oxygen captures conduction-band electrons and forms a surface depletion layer, while the dominant chemisorbed species progressively evolves with temperature, generally from molecular O_2^- toward atomic O^- and, at sufficiently high temperatures, O^{2-}, thereby modifying the surface charge state and its interaction with NH_3 (Takata et al., 1976). Because the electric field and current pathway of T-IDT are concentrated near this gas-active surface, changes in oxygen-species population, adsorption/desorption equilibrium, and NH_3–oxygen reaction kinetics can strongly alter the balance of surface charge transfer and consequently the sign of the measured resistance change. In contrast, the greater contribution of subsurface/bulk transport in B-IDT and H-IDT reduces their sensitivity to such surface-state transitions, resulting in a more stable response polarity across the investigated temperature range.

It should be noted that relative humidity was not intentionally varied or independently controlled in the present study. Dry synthetic air was used as the carrier and reference gas under identical gas-delivery conditions for all three configurations. Humidity can influence MOS gas-sensing behavior because adsorbed water may alter

GU J Sci, Part A | 13(3) 1239-1257 (2026) | 10.54287/gujsa.1979919

the baseline resistance and compete with oxygen and target-gas molecules for surface adsorption sites (Tereshkov et al., 2024). Nevertheless, maintaining the same experimental conditions across all devices enables a direct comparison of electrode-position effects without introducing humidity as an additional variable. Similarly, the present study focuses specifically on NH_3 as the target analyte; therefore, selectivity against interfering gases was not evaluated. Further studies under controlled humidity and in the presence of potential interfering gases will be necessary to establish the performance of these configurations under practical NH_3-sensing conditions.

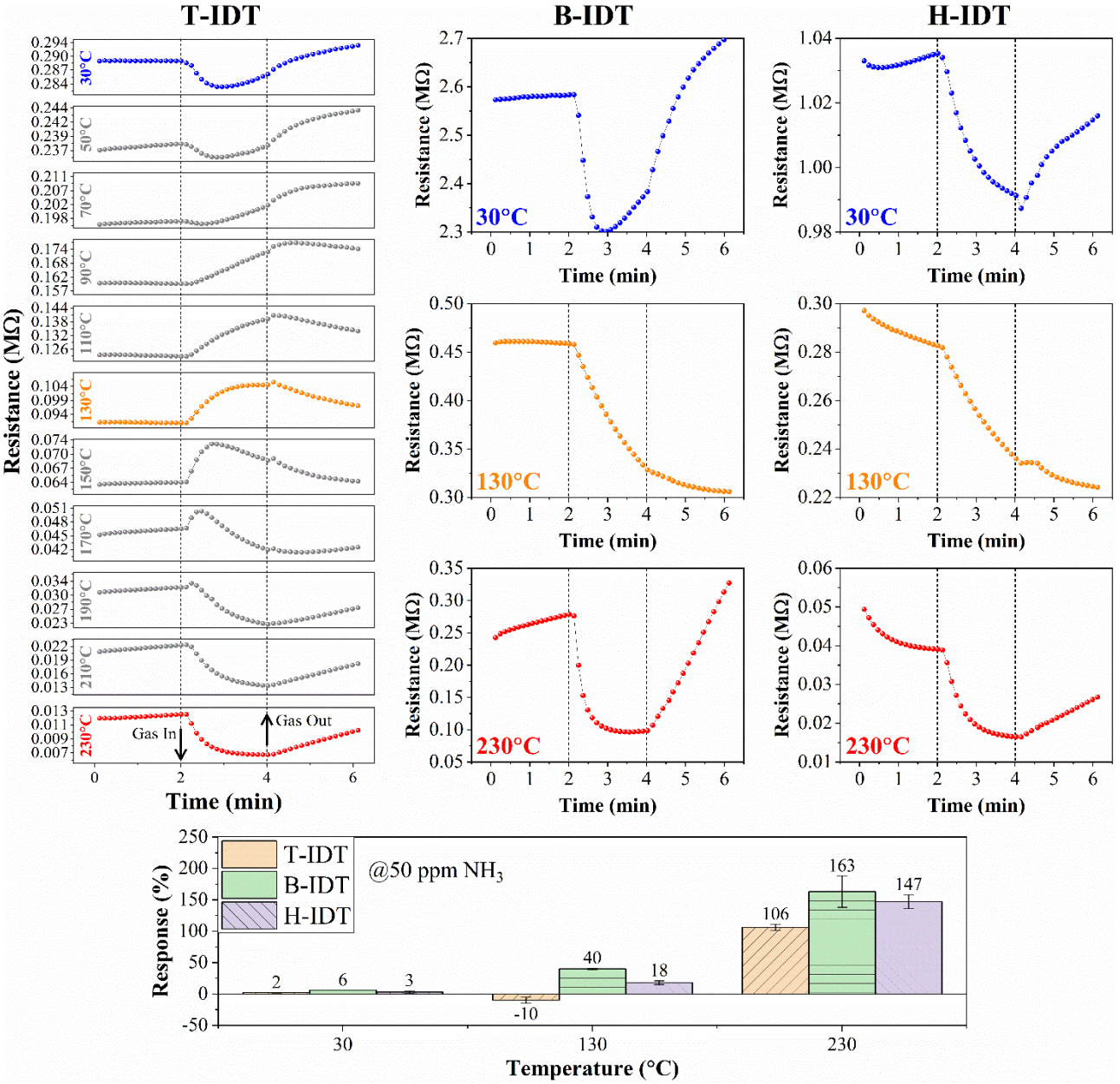

Figure 4. *Representative transient resistance responses of the T-IDT, B-IDT, and H-IDT ZnO sensors toward 50 ppm NH_3 over the investigated temperature range (30–230°C), together with a comparison of their sensing responses at selected temperatures. The response values in the histogram represent the mean of three repeated measurements on the same device, with error bars indicating the corresponding standard deviation.*

GU J Sci, Part A | 13(3) 1239-1257 (2026) | 10.54287/gujsa.1979919

Figure 5 further evaluates the cyclic repeatability and concentration-dependent sensing behavior of the three electrode configurations at 230°C. During five consecutive exposure–recovery cycles at 50 ppm NH_3, no substantial baseline drift was observed, while the initially higher response progressively decreased slightly and approached a more stable level over successive cycles. Such cycle-dependent evolution has also been reported in metal-oxide gas sensors, ranging from progressive stabilization during repeated exposure to persistent cycle-to-cycle variations (Almaev et al., 2025; Torkamani et al., 2025). The concentration-dependent measurements from 5 to 200 ppm showed a systematic increase in response for all configurations, with approximately linear calibration relationships (R^2 = 0.93, 0.96, and 0.89 for T-IDT, B-IDT, and H-IDT, respectively). These measurements demonstrate improved response stability after the initial cycling period and confirm that the distinct response characteristics associated with electrode positioning persist across the investigated NH_3 concentration range.

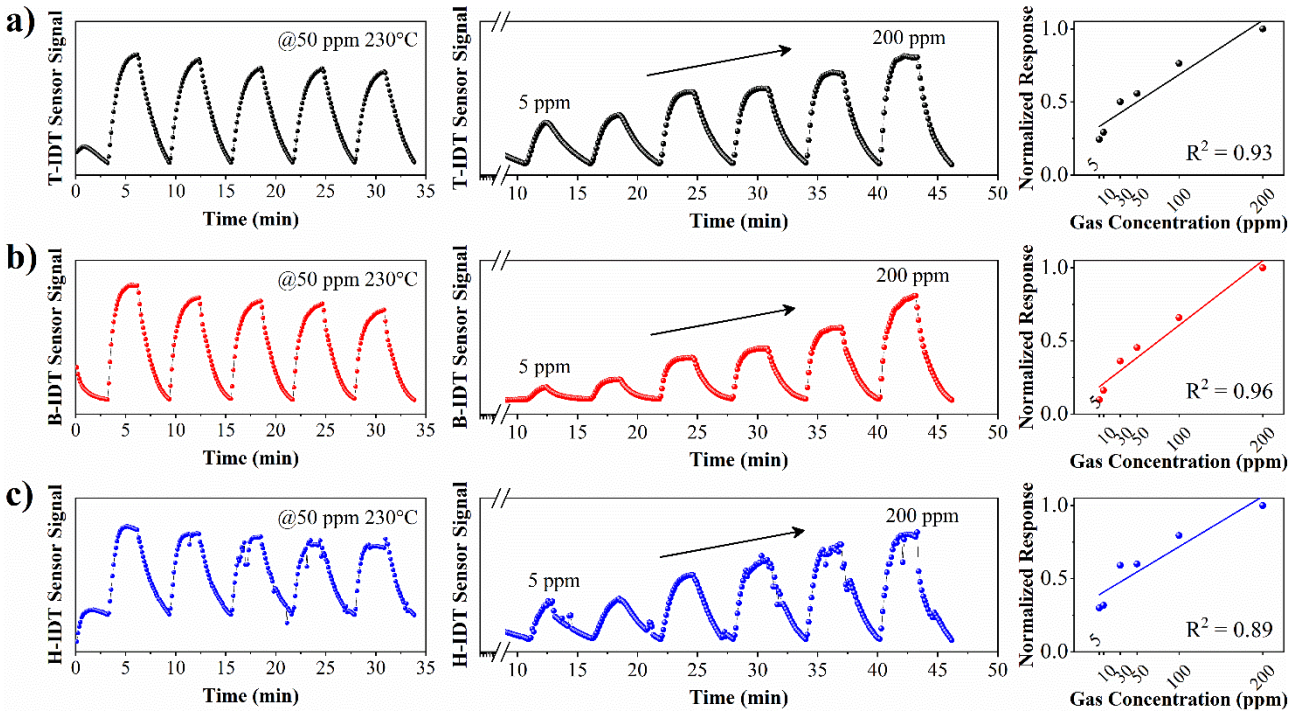

Figure 5. *Repeatability and concentration-dependent NH_3-sensing characteristics of* ***a)*** *T-IDT,* ***b)*** *B-IDT, and* ***c)*** *H-IDT sensors at 230°C, showing five consecutive response cycles at 50 ppm, dynamic responses to 5–200 ppm NH_3, and the corresponding normalized response–concentration relationships. The response values were normalized to the corresponding maximum response obtained for each electrode configuration.*

Figure 6 presents a conceptual representation of the expected electric-field distribution and dominant charge-transport pathways associated with the three IDT configurations investigated in this work; therefore, the illustrated field distributions should be interpreted qualitatively rather than as quantitatively simulated profiles. Upon application of a bias voltage, electric-field lines are expected to develop between opposing IDT fingers, generating conduction pathways within the ZnO sensing layer through which gas-induced conductivity changes are electrically detected. Electrode positioning is expected to modify the spatial distribution of these fields and, consequently, the relative contributions of near-surface and bulk transport. In the T-IDT configuration (Figure 6a), the electric field may be concentrated predominantly in the upper region of the ZnO

GU J Sci, Part A | 13(3) 1239-1257 (2026) | 10.54287/gujsa.1979919

layer, with some field extending into the surrounding medium owing to the dielectric contrast between air and ZnO. This geometry can therefore favor more direct electrical sampling of conductivity changes in the gas-active near-surface region. In contrast, the B-IDT configuration (Figure 6b) may involve a greater contribution from field and current pathways extending through the ZnO layer from the buried electrode/ZnO interface, thereby increasing the relative contribution of subsurface and bulk transport to the measured response. The H-IDT configuration (Figure 6c), with opposing electrodes located on different sides of the film, can be expected to produce mixed lateral and vertical field components involving both near-surface and subsurface regions. This qualitative picture is consistent with the experimental DC, impedance, and gas-sensing results, in which the B-IDT sensor exhibited the highest NH_3 response, while the three configurations showed distinct, temperature-dependent response/recovery dynamics. These findings highlight that, beyond the intrinsic properties of the sensing material, the spatial distribution of the electric field imposed by electrode configuration may represent an important device-level parameter for tailoring charge transport and gas-sensing behavior in thin-film sensors.

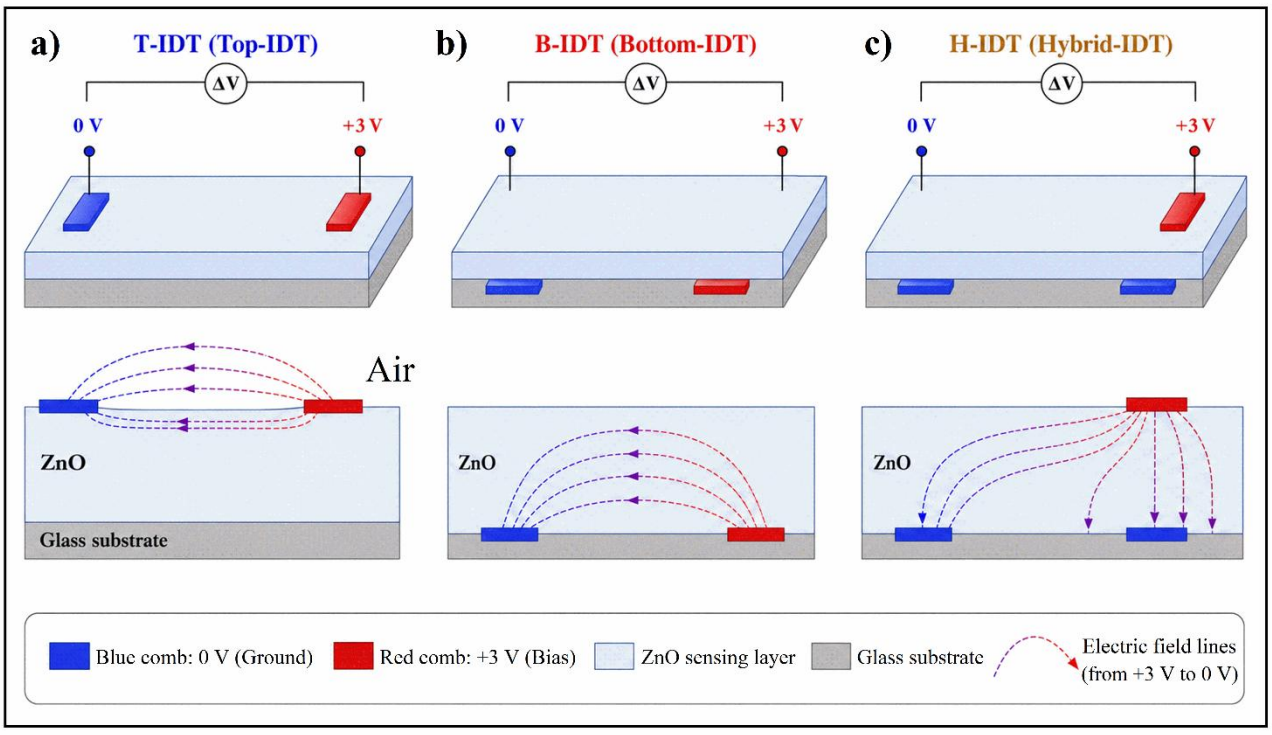

Figure 6. *Conceptual schematic of the expected electric-field and charge-transport pathways for the* ***a)*** *T-IDT,* ***b)*** *B-IDT, and* ***c)*** *H-IDT configurations.*

The proposed transport model also provides a qualitative link between charge transport and the gas-sensing mechanism. Since NH_3 sensing in ZnO originates from surface reactions with chemisorbed oxygen species, the resulting change in electron concentration is expected to influence the electrically active region sampled by the IDT-generated electric field. Consequently, the measured sensing response depends not only on the magnitude of the surface reaction but also on how effectively the resulting conductivity modulation is sampled by the electrode-defined current pathway. This provides a plausible explanation for why the B-IDT

GU J Sci, Part A | 13(3) 1239-1257 (2026) | 10.54287/gujsa.1979919

configuration, despite its higher electrical resistance, exhibits the highest sensing response, whereas the T-IDT configuration shows a lower response magnitude and distinct dynamic behavior.

4. CONCLUSION

The present study demonstrates that electrode positioning is an important device-level parameter governing the electrical transport and NH_3-sensing characteristics of ZnO thin films, even when the sensing material, electrode geometry, and fabrication conditions are maintained identical. Structural and compositional analyses confirm the formation of polycrystalline wurtzite ZnO with homogeneous elemental distribution and continuous film morphology. Electrical measurements reveal approximately linear I–V characteristics, while the T-IDT, H-IDT, and B-IDT devices exhibit markedly different baseline resistances. Equivalent-circuit analysis of the impedance spectra further demonstrates configuration-dependent resistive and relaxation behavior, with the buried B-IDT configuration exhibiting the most complex electrical response. Despite its higher resistance, B-IDT consistently provides the highest NH_3 response, reaching 163% at 230°C, compared with 147% and 106% for H-IDT and T-IDT, respectively. Quantitative t_{90} analysis further shows that the fastest response and recovery are not consistently associated with a particular electrode configuration, but vary with operating temperature. Furthermore, repeated exposure–recovery measurements demonstrate stabilization after initial cycling, while measurements over 5–200 ppm NH_3 confirm a systematic concentration-dependent response for all three configurations, with B-IDT exhibiting the strongest linear response–concentration relationship ($R^2 = 0.96$). Collectively, the results indicate that electrode positioning modifies how gas-induced conductivity changes within the ZnO layer are electrically sampled, thereby producing a practical trade-off among response magnitude, baseline resistance, and dynamic behavior. As a practical design guideline, B-IDT is advantageous when maximizing response magnitude is prioritized, whereas configurations exhibiting shorter response/recovery times may be preferable for real-time monitoring; H-IDT provides an alternative pathway combining top- and bottom-side current collection. Thus, electrode positioning offers a simple strategy for tailoring resistive gas-sensor performance without additional modification of the sensing material.

AUTHOR CONTRIBUTIONS

AI Exclusion: AI tools are strictly prohibited from being listed as authors.

Legal Consent: All human authors confirm they have reviewed and legally accepted the final version under the **CC BY-SA 4.0** framework.

ACKNOWLEDGEMENT

The author gratefully acknowledges Prof. Dr. Selim Acar for providing access to the chemical synthesis and gas-sensing measurement facilities at Gazi University.

CONFLICT OF INTEREST

The author declares no conflict of interest.

GU J Sci, Part A | 13(3) 1239-1257 (2026) | 10.54287/gujsa.1979919

REFERENCES

Ajjaq, A., Bulut, F., Ozturk, O., & Acar, S. (2024). Advanced NH_3 Detection by 1D Nanostructured La:ZnO Sensors with Novel Intrinsic p–n Shifting and Ultrahigh Baseline Stability. *ACS Sensors*, *9*(2), 895–911. https://doi.org/10.1021/acssensors.3c02256

Almaev, A. V., Karipbayev, Z. T., Kakimov, A. B., Yakovlev, N. N., Kukenov, O. I., Korchemagin, A. O., Akmetova-Abdik, G. A., Kumarbekov, K. K., Zhunusbekov, A. M., Mochalov, L. A., Slapovskaya, E. A., Korusenko, P. M., Koroleva, A. V., Zhizhin, E. V., & Popov, A. I. (2025). High-Temperature Methane Sensors Based on $ZnGa_2O_4$:Er Ceramics for Combustion Monitoring. *Technologies*, *13*(7), 286. https://doi.org/10.3390/technologies13070286

Balasubramani, V., Sureshkumar, S., Subba Rao, T., & Sridhar, T. M. (2019). Impedance Spectroscopy-Based Reduced Graphene Oxide-Incorporated ZnO Composite Sensor for H_2S Investigations. *ACS Omega*, *4*(6), 9976–9982. https://doi.org/10.1021/acsomega.9b00754

Barin, Ö., Ajjaq, A., Çağırtekin, A. O., Karaduman Er, I., Yıldırım, M. A., Ateş, A., & Acar, S. (2022). Pivotal Role of Nucleation Layers in the Hydrothermally-Assisted Growth of ZnO and its H_2 Gas Sensing Performance. *Sensors and Actuators B: Chemical*, *371*, 132499. https://doi.org/10.1016/j.snb.2022.132499

Boukamp, B. A. (2001). Interpretation of an 'Inductive Loop' in the Impedance of an Oxygen Ion Conducting Electrolyte/Metal Electrode System. *Solid State Ionics*, *143*(1), 47–55. https://doi.org/10.1016/S0167-2738(01)00832-3

Cao, J., Yang, Z., Zhang, W., Wang, W., Zhang, R., Li, Y., & Chen, L. (2025). A Wide-Range Resistance-to-Frequency Read-Out Circuit for Resistive Gas Sensors. *International Journal of Circuit Theory and Applications*, *53*(11), 6152–6161. https://doi.org/10.1002/cta.4534

Chen, T.-Y., Chen, H.-I., Hsu, C.-S., Huang, C.-C., Wu, J.-S., Chou, P.-C., & Liu, W.-C. (2015). Characteristics of ZnO Nanorods-Based Ammonia Gas Sensors with a Cross-Linked Configuration. *Sensors and Actuators B: Chemical*, *221*, 491–498. https://doi.org/10.1016/j.snb.2015.06.122

Chuong, K. Y., Liu, Y., Forbes, T., Frye, M. B., Graber, L., & Garten, L. M. (2026). Determining the Effect of Bismuth Oxide on the Microstructure and Electrical Response of Cold-Sintered ZnO Varistors. *Journal of the American Ceramic Society*, *109*(1), e70406. https://doi.org/10.1111/jace.70406

Cui, L., & Murray, E. P. (2015). Effect of Electrode Configuration on Nitric Oxide Gas Sensor Behavior. *Sensors*, *15*(9), 24573–24584. https://doi.org/10.3390/s150924573

Çağırtekin, A. O., & Acar, S. (2026). Room-Temperature Ammonia Sensing Performance of 1D ZnO/Si Nanorods: Influence of Zinc Precursors and Yttrium Doping Levels. *Sensors and Actuators B: Chemical*, *447*(1), 138801. https://doi.org/10.1016/j.snb.2025.138801

Demircan, G., Yalcin, S., Alivi, K., Ceyhan, G., Acikgoz, A., Balak, M. V., Aktas, B., & Das, R. (2022). The Effect of Co and Mn Co-Doping on Structural and Optical Properties of ZnO Thin Films. *Optical Materials*, *126*, 112163. https://doi.org/10.1016/j.optmat.2022.112163

Fioravanti, A., Marani, P., Morandi, S., Lettieri, S., Mazzocchi, M., Sacerdoti, M., & Carotta, M. C. (2021). Growth Mechanisms of ZnO Micro-Nanomorphologies and their Role in Enhancing Gas Sensing Properties. *Sensors*, *21*(4), 1331. https://doi.org/10.3390/s21041331

Hjiri, M., Algessair, S., Dhahri, R., Albargi, H. B., Ben Mansour, N., Assadi, A. A., & Neri, G. (2024). Ammonia Gas Sensors Based on Undoped and Ca-Doped ZnO Nanoparticles. *RSC Advances*, *14*(8), 5001–5011. https://doi.org/10.1039/D3RA08181H

Hsueh, T.-J., & Ding, R.-Y. (2022). A Room Temperature ZnO-NPs/MEMS Ammonia Gas Sensor. *Nanomaterials*, *12*(19), 3287. https://doi.org/10.3390/nano12193287

Huang, B.-R., Kathiravan, D., Hsieh, H.-R., & Saravanan, A. (2024). Heterostructure Interfaces and Dimensionally Transformed GaO/ZnO Nanostructures for Room-Temperature Hydrogen Gas Sensors. *International Journal of Hydrogen Energy*, *64*, 889–895. https://doi.org/10.1016/j.ijhydene.2024.03.273

Huang, C.-Y., Juan, K.-Y., Guo, P.-H., Wu, Y.-R., Kao, S.-F., & Liao, S.-Y. (2024). Self-Powered InGaZnO Ozone Gas Sensors Based on a Metal–Semiconductor–Metal Structure with Asymmetric Interdigitated Electrodes. *ACS Applied Electronic Materials*, *6*(3), 2075–2083. https://doi.org/10.1021/acsaelm.4c00171

Konuk Ege, G., İrge, M., & Aydın, E. (2026). Design and Prototype Development of a Sensor Structure for Gas Sensing Applications. *Journal of Materials and Mechatronics: A*, *7*(1), 76–86. https://doi.org/10.55546/jmm.1808591

Lee, S. P. (2017). Electrodes for Semiconductor Gas Sensors. *Sensors*, *17*(4), 683. https://doi.org/10.3390/s17040683

Mokrushin, A. S., Dmitrieva, S. A., Simonenko, N. P., Averin, A. A., Gorobtsov, P. Y., Zvyagina, A. I., & Simonenko, E. P. (2025). Influence of AACVD Temperature on the Microstructural and Gas Sensing Properties of ZnO Thin Films. *Russian Journal of Inorganic Chemistry*, *70*(10), 1391–1405. https://doi.org/10.7868/S3034560X25100172

Öztürk, S., Kılınç, N., & Öztürk, Z. Z. (2013). Fabrication of ZnO Nanorods for NO_2 Sensor Applications: Effect of Dimensions and Electrode Position. *Journal of Alloys and Compounds*, *581*, 196–201. https://doi.org/10.1016/j.jallcom.2013.07.063

Plecenik, T., Moško, M., Haidry, A. A., Ďurina, P., Truchlý, M., Grančič, B., Gregor, M., Roch, T., Satrapinskyy, L., Mošková, A., Mikula, M., Kúš, P., & Plecenik, A. (2015). Fast Highly-Sensitive Room-Temperature Semiconductor Gas Sensor Based on the Nanoscale Pt–TiO_2–Pt Sandwich. *Sensors and Actuators B: Chemical*, *207*(A), 351–361. https://doi.org/10.1016/j.snb.2014.10.003

Prajesh, R., Goyal, V., Saini, V., Bhargava, J., Sharma, A., & Agarwal, A. (2018). Effect of IDE Placement on Response in Metal Oxide Gas Sensors. *Materials Research Express*, *5*(9), 096415. https://doi.org/10.1088/2053-1591/aad728

Schroder, D. K. (2006). *Semiconductor Material and Device Characterization* (3rd Ed.). Wiley. https://doi.org/10.1002/0471749095

Soltabayev, B., Yergaliuly, G., Ajjaq, A., Beldeubayev, A., Acar, S., Bakenov, Z., & Mentbayeva, A. (2022). Quick NO Gas Sensing by Ti-Doped Flower–Rod-Like ZnO Structures Synthesized by the SILAR Method. *ACS Applied Materials & Interfaces*, *14*(36), 41555–41570. https://doi.org/10.1021/acsami.2c10055

Sze, S. M., & Ng, K. K. (2007). *Physics of Semiconductor Devices* (3rd Ed.). Wiley. https://doi.org/10.1002/0470068329

Takata, M., Tsubone, D., & Yanagida, H. (1976). Dependence of Electrical Conductivity of ZnO on Degree of Sintering. *Journal of the American Ceramic Society*, *59*(1–2), 4–8. https://doi.org/10.1111/j.1151-2916.1976.tb09374.x

Tereshkov, M., Dontsova, T., Saruhan, B., & Krüger, S. (2024). Metal Oxide-Based Sensors for Ecological Monitoring: Progress and Perspectives. *Chemosensors*, *12*(3), 42. https://doi.org/10.3390/chemosensors12030042

Torkamani, R., Aslibeiki, B., Salari, S., Azizi, H., Peddis, D., & Sarkar, T. (2025). High-Performance Hydrogen Gas Sensor Based on Ag-Incorporated ZnO Nanoparticles. *Scientific Reports*, *15*, 38390. https://doi.org/10.1038/s41598-025-22222-9

Vuong, N. M., Chinh, N. D., Huy, B. T., & Lee, Y.-I. (2016). CuO-Decorated ZnO Hierarchical Nanostructures as Efficient and Established Sensing Materials for H_2S Gas Sensors. *Scientific Reports*, *6*, 26736. https://doi.org/10.1038/srep26736

Wei, H.-L., Kumar, P., & Yao, D.-J. (2020). Printed Resistive Sensor Array Combined with a Flexible Substrate for Ethanol and Methane Detection. *ECS Journal of Solid State Science and Technology*, *9*(11), 115008. https://doi.org/10.1149/2162-8777/ab9fe6